THE JOURNAL OF PHYSICAL CHEMISTRY LETTERS
A JOURNAL OF THE AMERICAN CHEMICAL SOCIETY

pubs.acs.org/JPCL

Letter

Atomistic Description of the Impact of Spacer Selection on Two-Dimensional (2D) Perovskites: A Case Study of 2D Ruddlesden–Popper $CsPbI_3$ Analogues

Robert Stanton and Dhara J. Trivedi*

Cite This: *J. Phys. Chem. Lett.* 2022, 13, 12090–12098

Read Online

ACCESS | Metrics & More | Article Recommendations | Supporting Information

ABSTRACT: Inorganic $CsPbI_3$ perovskites have become desirable for use in photovoltaic devices due to their excellent optoelectronic properties and increased resilience to thermal degradation compared to organic–inorganic perovskites. An effective strategy for improving both the performance and the phase stability of $CsPbI_3$-based perovskites is through introducing a diverse set of spacing cations separating inorganic layers in their two-dimensional (2D) analogues. In this work, $CsPbI_3$-based 2D Ruddlesden–Popper perovskites were investigated using three aromatic spacers, 2-thiophenemethylamine (ThMA), 2-thiopheneformamidine (ThFA), and benzylammonium, fluorinated through *para* substitution (pFBA). Our findings highlight the importance of the local bonding environment between organic spacers and the PbI_6 octahedra. Additionally, we demonstrated the importance of energetic alignment between electronic states on spacing cations and inorganic layers for optoelectronic applications. Furthermore, thermoelectric performance was investigated revealing a preference for p-type ThFA and n-type ThMA and pFBA configurations.

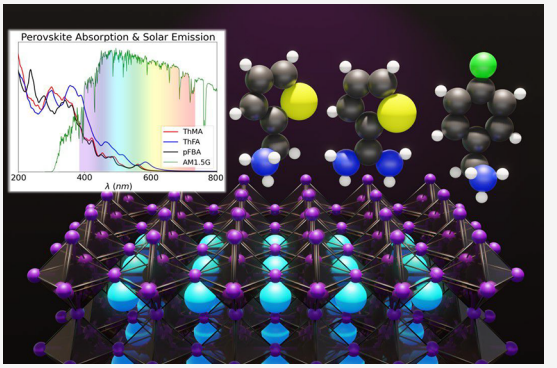

Perovskites as a platform for solar energy harvesting are a well-established and thoroughly investigated class of materials that vary broadly in building components, applications, and photovoltaic (PV) performance.[1−5] Research outcomes from perovskite solar cells have led to a dramatic increase in power conversion efficiency (PCE), with recent improvements reaching to 25.7%.[6] Bulk perovskites have a chemical formula of ABX_3, for which an A:B charge ratio of 1:2 is most common, where A is a monovalent organic or inorganic cation, B is Pb, Sn, or Ge, and X is a halogen anion. However, the primary drawback of bulk perovskites for solar energy applications remains their poor long-term stability, which leads to the required maintenance or disposal of damaged cells, and the leakage of building components into the environment.[7−9] The latter is particularly problematic for the best performing perovskites that have Pb as the B cation, and extensive effort is currently being dedicated to mitigating this lead leakage.[10−14] To improve the stability of ABX_3 perovskites while maintaining PV performance, mixed metal double perovskites and two-dimensional perovskites (2DPKs) have emerged as primary candidates for the next generation of highly efficient solar energy-harvesting materials.[15−20] Two-dimensional (2D) analogues of bulk perovskites stand out as a particularly promising platform for increasing both the stability and the tunability of perovskite solar cells.[21−23] 2D materials more broadly are unrivaled in their ability to realize highly tunable electronic structures, variable layered arrangements, and confinement effects associated with an electronic decoupling of adjacent inorganic layers.[24−28] 2DPKs come in three primary phases: (1) the 2D Ruddlesden–Popper (2DRP) phase, where adjacent layers exhibit a half-unit cell shift along both in-plane directions, (2) the Dion Jacobson phase, where adjacent layers are stacked directly atop one another, and (3) the alternating cation phase, where adjacent layers exhibit a half-unit cell shift along one in-plane direction.[15]

2DPKs consist of thin perovskite layers separated by long organic spacing cations, which spatially and electronically separate the adjacent inorganic layers.[29−32] The 2DRP phase, the focus of this study, has a chemical formula of $A'_2A_{n-1}B_nX_{3n+1}$, where A, B, and X remain the same as in their bulk counterpart, A′ represents a monovalent organic spacer, and n represents the number of BX_6 octahedra per inorganic layer. 2DPKs exhibit significantly improved stability compared to that of their bulk counterparts, but this often comes at the cost of PV performance because of significantly increased band gaps.[33] Thus, to generate stable perovskite solar cells with favorable optoelectronic performance, research

Received: November 14, 2022
Accepted: December 12, 2022
Published: December 22, 2022

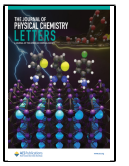

https://doi.org/10.1021/acs.jpclett.2c03463
J. Phys. Chem. Lett. 2022, 13, 12090–12098

involving 2DPKs aims to balance these two factors while simultaneously exploiting properties available exclusively to the 2D materials, such as the Rashba effect.[34−37] Additionally, the choice of the A′ spacing cation has been shown to affect characteristics ranging from the ease of synthesis and resultant crystal orientations to phase stability and even optoelectronic performance.[38−41] In this Letter, we characterize the role of this A′ spacing cation to further elucidate its effects on the resulting geometry, electronic structure, and thermoelectric (TE) and PV properties of 2DRP $CsPbI_3$ analogues.

$CsPbI_3$ perovskites are closely related to the prototypical $MAPbI_3$ perovskite but differ in that the organic methylammonium cation is replaced with an inorganic Cs^+ cation, which removes degrees of freedom such as A cation orientation and results in a peak PCE of 21%. Although 2D $CsPbI_3$ analogues have attracted significant interest in recent years, their performance is poorer than that of their mixed organic−inorganic counterparts. Experimental work by Xu et al. employing 2-thiophenemethylamine (ThMA) and 2-thiopheneformamidine (ThFA) spacing cations demonstrated the highest PCE of 2D $CsPbI_3$ analogues at 16%.[42] Additionally, Yan et al. recently investigated the inclusion of fluorinated aromatic spacers in 2D $MaPbI_3$ analogues; their work uncovered remarkable stability and optoelectronic performance particularly for *para*-substituted fluoro-benzylammonium (pFBA) spacers.[43] While these systems have been synthesized experimentally and established as a potential platform for high-performance 2DPKs, a full computational investigation at the atomistic level to elucidate factors responsible for this increased performance has yet to be conducted. In this study, we further characterize the role that aromatic organic spacing cations play in 2D $CsPbI_3$ analogues by employing *ab initio* calculations to investigate key differences emerging from the usage of ThMA, ThFA, and pFBA spacers in the n = 2 2DRP phase of $CsPbI_3$ perovskite analogues.

The role played by the organic A′ spacing cations that separate, both spatially and electronically, adjacent inorganic layers in 2DPKs is largely dependent on their size, orientation, mutual interactions between spacers, and organic−inorganic interactions at the spacer−perovskite interface.[44−46] These A′ cations come with a broad range of chemical diversity. In the study presented here, ThMA and ThFA are representative of monoammonium and diammonium aromatic spacing cations, respectively, with the aromatic portion consisting of a thiophene heterocycle, and the pFBA spacer is a monoammonium aromatic spacer with a *para*-substituted fluorine atom on the benzene ring. The geometries of the n = 2 2DRP phases of the ThMA-, ThFA-, and pFBA-containing perovskites are presented in Figure 1. Figure S1 shows the same geometries with another orientation for the sake of clarity. The arrangement of aromatic spacers in 2DPKs is of particular geometric interest as the potential for strong π interactions may result in packing arrangements that can drastically affect the stability, performance, and longevity of the perovskite.[47] In the case of ThMA, we find a T-shaped π-stacking mode, and the orientation of the heterocycle alternates approximately 90° for each spacer in the unit cell (Figure S3). A similar alternating arrangement is found in the case of pFBA; however, because π interactions are absent entirely, this results in a much more irregular arrangement. The mode of NH−I interactions between the spacer and inorganic layer is very similar in the ThMA- and pFBA-containing perovskites; the ammonium group exhibits two strong NH−I interactions

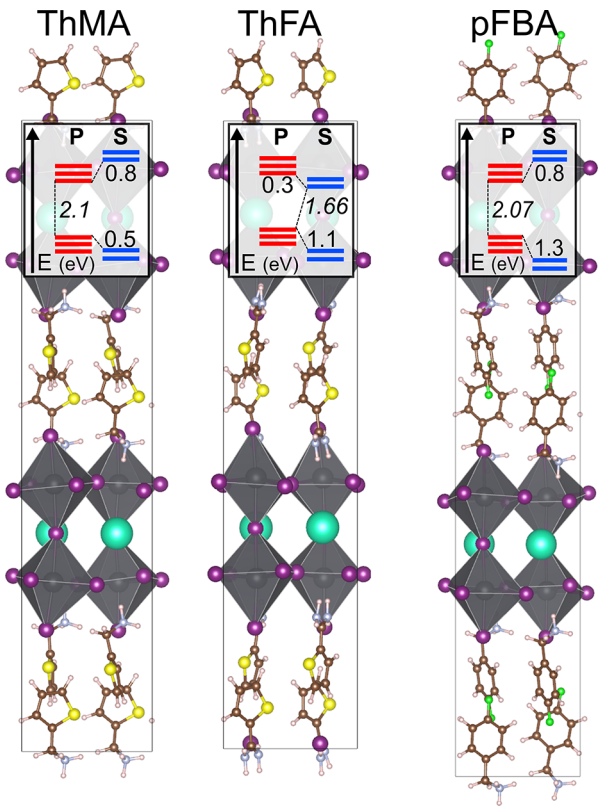

Figure 1. Unit cells for the ThMA, ThFA, and pFBA 2DRP $CsPbI_3$ analogues. Schematic diagrams of the band alignment of the perovskite (P) and spacer (S) are placed in the topmost inorganic layer with the optical band gaps italicized.

(∼2.6 Å) and two weaker NH−I interactions (≤3 Å, with a much smaller NH−I bond angle). Additionally, weaker CH−I interactions are present in the ThMA and pFBA systems that contain CH_2 coordinated to the terminal ammonia group. Representative examples of NH−I interactions are presented in Figure S2. The most unique interaction, however, comes from the ThFA spacers, which were found experimentally by Xu et al. to have the highest PCE of any 2D $CsPbI_3$ analogue to date. We find that the diammonium cation that penetrates the inorganic layer results in strong anisotropy in terms of the in-plane lattice parameters. NH−I interactions are formed by both NH_2 groups, which come in the form of strong NH−I interactions (<2.8 Å) and/or longer NH−I interactions (<3.2 Å). The cell is significantly elongated along the NH_2−C−NH_2 bond of the FA group with cell parameters of 8.67 and 9.30 Å for the a and b directions, respectively. Quantitatively, this corresponds to a 6.7% difference between in-plane cell parameters, compared with 1.2% and 0.2% in the ThMA- and pFBA-containing perovskites, respectively. This also results in larger in-plane Pb−I−Pb bond angles of 159° in ThFA compared to angles of 147° and 146° for ThMA- and pFBA-containing perovskites, respectively. Additionally, the cell elongation corresponds to the more uniform stacking of the BX_6 octahedra where edges run nearly parallel with the unit cell (Figure S3), which commonly comes with a smaller band gap.[48] The strong NH−I binding modes and increased Pb−I−Pb angles in ThFA compared to those in ThMA correspond directly with predictions from a previous experimental study.[42] The full sets of cell parameters, atomic coordinates, and geometric parameters of bond lengths and bond angles are

https://doi.org/10.1021/acs.jpclett.2c03463
J. Phys. Chem. Lett. 2022, 13, 12090−12098

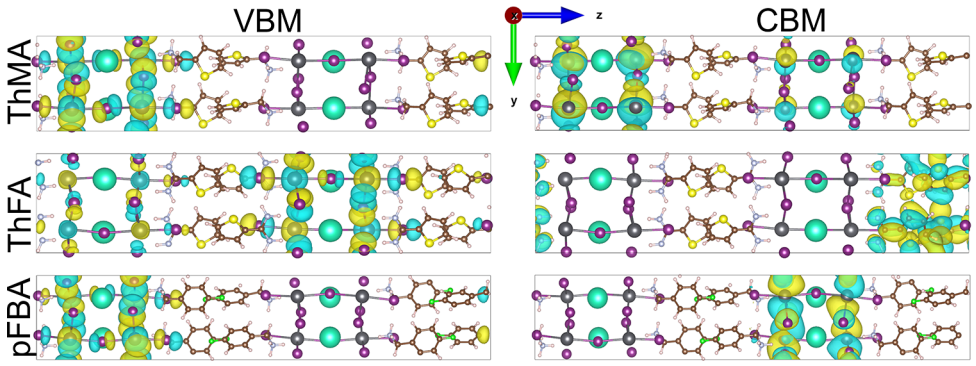

Figure 2. Kohn−Sham orbitals corresponding to the valence band maximum (VBM) and conduction band minimum (CBM) of the ThMA-, ThFA-, and pFBA-containing perovskite systems. The CBM of ThFA displays the states introduced that localize to the organic spacer.

presented in Tables S1 and S2, respectively. Another unique characteristic of the ThFA-containing perovskite is that the diammonium cations that elongate the *b* dimension of the unit cell strongly restrict the free rotation of their respective heterocycles. This results in the only parallel arrangement of aromatic rings of the three spacers used in the study. The parallel arrangement leads to a staggered π-stacking mode between the aromatic rings, which may be desirable experimentally in terms of the resilience of solar cells to moisture penetration and charge transport properties.[49,50] Figures S1 and S2 depict these NH−I interactions and packing arrangements of the A′ cations. The subsequent discussion focuses on how these geometric properties of the ThMA-, ThFA-, and pFBA-containing perovskites translate to differences at the electronic structure level.

Upon examining the electronic structures of the ThMA-, ThFA-, and pFBA-containing perovskites, we found that geometric similarities observed between ThMA and pFBA hold while ThFA is distinguishable in a few key ways. ThMA and pFBA exhibit direct band gaps of 2.10 and 2.07, eV respectively, which upon examination of the projected density of states (PDOS) (Figure S3) correspond to the direct I(p)−Pb(p) transition that is commonly found in perovskite solar cells.[51,52] In the case of ThFA, however, we find an indirect Γ−Y transition. The PDOS and CBM orbital (Figure S4 and Figure 2) of ThFA demonstrate that the energetic alignment of bands introduced through the spacer results in midgap states that localize the new band edges to the organic spacer molecules, thereby reducing the band gap to 1.66 eV. We also carried out calculations including spin−orbit coupling (SOC) to further investigate the relative placement of these bands. Upon inclusion of SOC, ThMA, pFBA, and ThFA, all exhibit a direct transition at the Γ point. We attribute the drastic change upon inclusion of SOC in the ThFA-containing perovskite to the fact that the spin splitting associated with SOC is an effect restricted to the heavy atoms in the system (here largely I and Pb, as Cs does not contribute electronic states near the band gap). Consequently, conduction bands that are largely Pb(6p) in character penetrate the relatively flat bands localized to the spacer, restoring the p−p transition within a given inorganic layer. We also note that all organic spacers entirely decouple the inorganic layers as evidenced by both the flat bands along the Γ−Z direction and the degenerate pairs of band edges in the band structures. This demonstrates that a nearly identical electronic structure is present in the two inorganic layers, which are required per unit cell to generate the 2DRP stacking arrangement.

Consideration of the electronic band structures in Figure 3 reveals another key observation relevant to the potential spintronic applications of 2DPKs. The color map of the SOC band structures corresponds to the spin character along the *z* direction with 1 (−1) corresponding to *z* (−*z*), computed as $s_{kn} = \langle kn|\sigma_z|kn\rangle$, where *k* and *n* represent the *k* point and band index, respectively. In Figure S4, we compute the band structure more densely along the X−Γ−Y path, where the hallmark of Rashba split bands can be clearly seen, with the shifting of the vertex of the split bands away from the Γ point, together with the inverted spin character of the VBM/CBM as the X−Γ−Y path is traversed. As we have noted in our previous work, Rashba splitting is very sensitive to geometric changes in the perovskite system owing to the strong spatially localized effects of SOC.[35] This paves the way for modulating the nature of excitations that are mediated by direct photoexcitation in the visible range, as demonstrated by Wang et al.[52] The correspondence between spatial and electronic degrees of freedom can even be seen in the case of ThFA, where the Γ−Y direction exhibits significantly stronger Rashba spin splitting than the Γ−X direction, in direct relation to the strong anisotropy previously discussed regarding the in-plane cell parameters.

To analyze the optoelectronic performance of the 2DPKs, we computed the absorption coefficient from the real and imaginary parts of the dielectric function at the non-SOC level (Figure 4).[53] We observe a long tail in the absorption spectra for the ThMA and pFBA perovskites owing to the strongly dispersive band edges, and a slightly more abrupt onset in the ThFA perovskite owing to the flat bands that are found to be localized on the organic spacer. Similarly, our results demonstrate the relatively higher absorption coefficients of the ThFA-containing perovskite over the visible range, further corroborating the experimental work by Xu et al.[42] Additionally, our results may explain the lack of distinct layer-dependent PL peaks obtained by Xu et al. in the ThFA-containing perovskite. Naturally, the midgap ThFA states would exhibit no layer dependence, thereby offering a first excitonic peak that exhibits much less layer dependence. The electronic structure of ThFA does raise the question of how the introduction of midgap states may correlate with a higher PCE. While the reduction of the band gap opens a broader range of the visible spectrum for absorption, this is likely not the only factor at play. While outside the scope of this investigation, future work will investigate the excitation dynamics and thereby the influence on the neutral exciton lifetime that is present in organic−inorganic transitions

https://doi.org/10.1021/acs.jpclett.2c03463
J. Phys. Chem. Lett. 2022, 13, 12090−12098

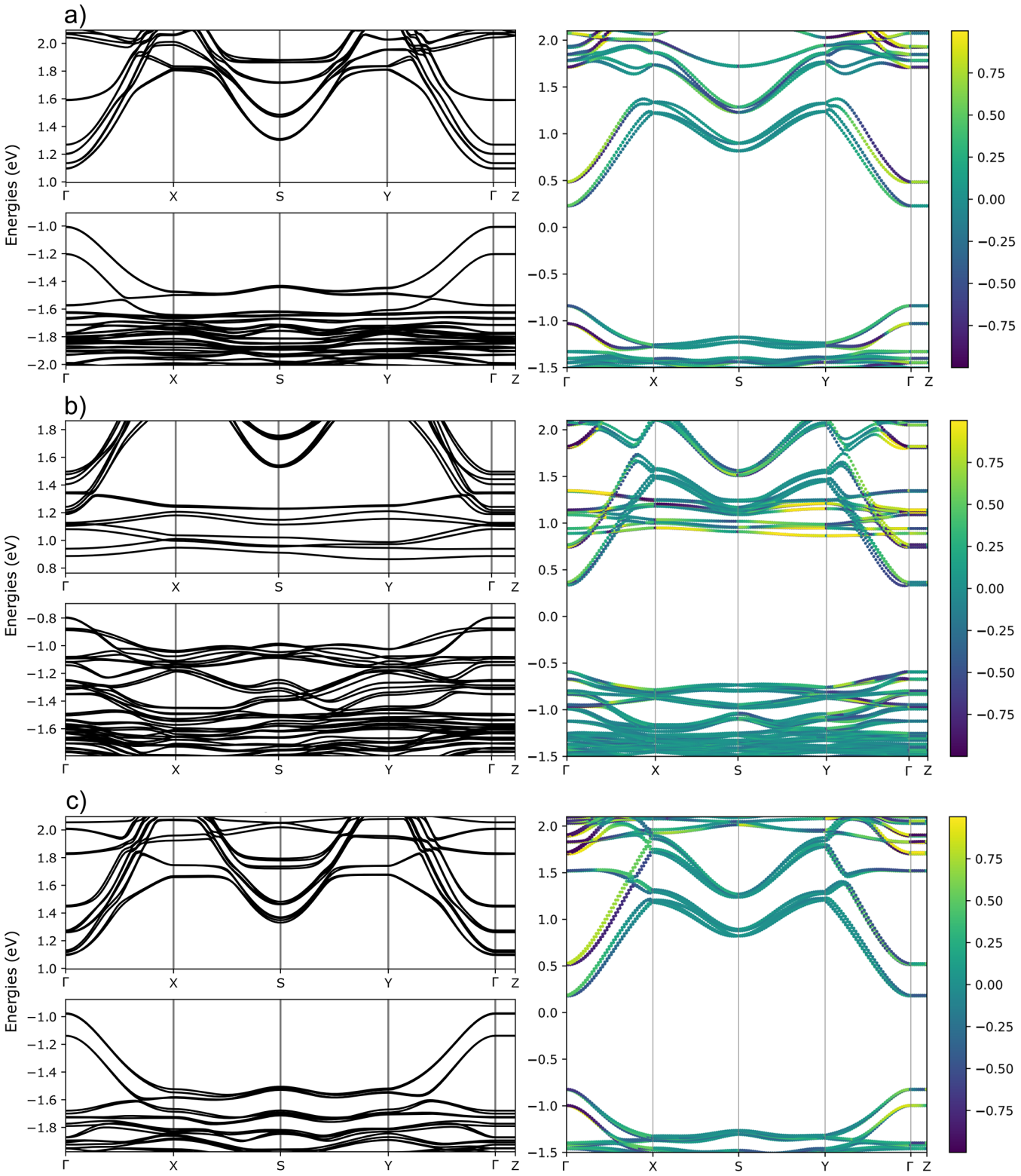

Figure 3. Band structures with (right) and without SOC (left) for the (a) ThMA, (b) ThFA, and (c) pFBA $CsPbI_3$ analogues. Spin character along the z axis is represented by the color map, with 1 (-1) corresponding to spin projection along the z $(-z)$ axis.

corresponding to the introduction of midgap states through careful spacer selection and band alignment.

As an improved PCE in perovskite solar cells has become increasingly difficult to obtain, the generation of hybrid PV-TE materials has emerged as a popular design strategy for improved perovskite-based solar energy-harvesting devices.[54−57] Hence, we evaluated the TE performance of the ThMA-, ThFA-, and pFBA-containing $CsPbI_3$ analogues through the lens of the Boltzmann transport equations as implemented in BoltzTraP2 under the constant relaxation time approximation. To more accurately describe the anisotropic nature of the transport properties, we computed relaxation

https://doi.org/10.1021/acs.jpclett.2c03463
J. Phys. Chem. Lett. 2022, 13, 12090−12098

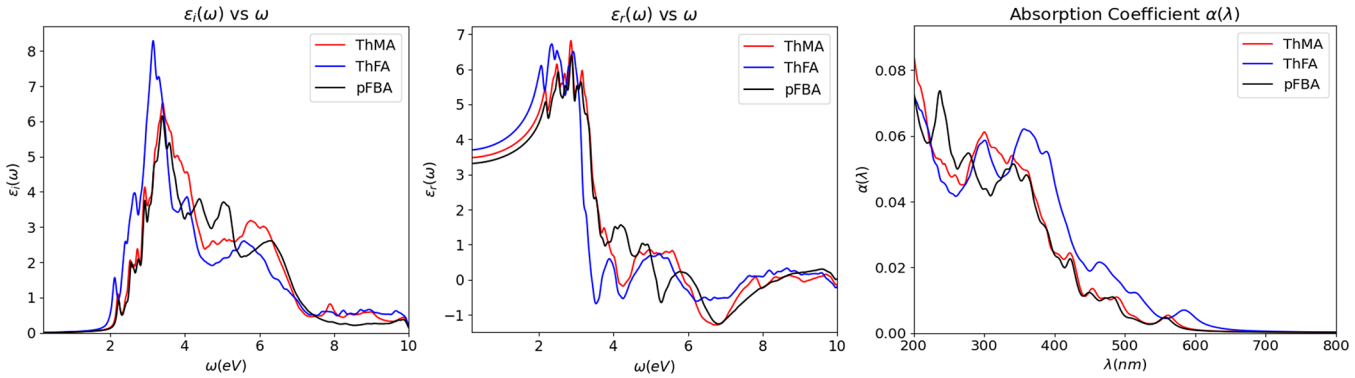

Figure 4. Real and imaginary parts of the dielectric function and absorption coefficient of the ThMA, ThFA, and pFBA 2DRP perovskites.

times from *ab initio* calculations in accordance with the deformation potential theory, which yields electron and hole mobilities according to

$$\mu_{n\nu} = \frac{2e\hbar^3 C_\nu^{2D}}{3k_b T E_{n\nu}^2 m_{n\nu}^*} \quad (1)$$

where $\mu_{n\nu}$ represents the charge carrier mobility, the index n corresponds to the carrier type, and ν corresponds to the Cartesian direction of the transport properties. C_ν^{2D} and $E_{n\nu}$ represent the in-plane stiffness constant and deformation potential, respectively (Figures S6–S8). The final quantity computed from *ab initio* electronic structure calculations is $m_{n\nu}^*$, which corresponds to the effective mass of holes and electrons along the two in-plane directions. Effective masses were computed both with and without SOC, and all values pertaining to eq 1 are listed in Tables 1 and 2. SOC effective masses were used for computation of the relaxation times $\tau_{n\nu} = \frac{\mu_{n\nu} m_{n\nu}^*}{e}$, as the curvature of the band structure is more accurate under its consideration due to the strongly dispersive I(p) and Pb(p) band edges present in these systems.

Table 1. Effective Masses Obtained from the Band Structures of the ThMA, ThFA, and pFBA $CsPbI_3$ Analogues with and without SOC

	m_{ex} (m_e)	m_{ey} (m_e)	m_{hx} (m_e)	m_{hy} (m_e)
ThMA	0.2270	0.3716	0.2969	0.3007
ThMA SOC	0.1717	0.1952	0.3894	0.2434
pFBA	0.2659	0.3181	0.2498	0.2598
pFBA SOC	0.3694	0.2690	0.2840	0.2662
ThFA	8.8397[a]	6.3375[a]	0.3073	0.2519
ThFA SOC	0.1341	0.1987	0.2066	0.2246

[a]The large difference between the ThFA calculations with and without SOC is attributed to the band reordering observed upon inclusion of SOC.

Seebeck coefficients (S), electrical conductivities (σ), and TE power factors ($S^2\sigma$) were computed as a function of carrier concentration for the ThMA, ThFA, and pFBA phases as shown in Figure 5. Peak S values for the three perovskites are roughly the same at ~1.5 mV K^{-1}, and S versus n trends are similar across the three perovskites with the exception of n-type ThFA. We attribute the slow decay of the Seebeck coefficient to the localization of the CB edges to the spacer that results in occupation of very flat bands (not lending themselves to efficient transport properties) in n-doped configurations. Similar qualitative trends in TE performance were found in the ThMA and pFBA perovskites because of similarities in their respective band structures from which the TE quantities were computed. Both exhibit significantly higher $S^2\sigma$ values in n-doped configurations, with the peak $S^2\sigma$ for carrier concentrations of $<10^{19}$ cm^{-3} being a factor of >2 higher in ThMA than in pFBA, which we attribute to the significantly lighter electrons with masses of 0.17 and 0.20 m_e in ThMA compared with 0.37 and 0.27 m_e in pFBA. Additionally, the direction of transport preferred in these two perovskites is different with ThMA exhibiting a peak $S^2\sigma$ value of 12.76 mW m K^{-1} along the x direction and pFBA a peak value of 4.88 mW m K^{-1} along the y direction. The ThFA-containing perovskites have the weakest TE performance with peak $S^2\sigma$ values of 2.68 and 1.38 mW m K^{-1} for transport along the x and y directions, respectively, both of which occur in the p-doped configurations. These findings support ThMA being the best candidate for exploiting TE properties to further increase the efficiency of 2DPKs used in solar cell devices. Additionally, these results highlight the necessity of obtaining structure-specific relaxation times for meaningful comparison of TE properties across multiple materials. Without these considerations, seemingly similar results would be obtained for systems that exhibit comparable band structures but differ greatly in nonequilibrium properties, as observed for ThMA and pFBA in this study.

Table 2. In-Plane Stiffness Constants, Deformation Potentials, Charge Carrier Mobilities, and Relaxation Times Computed from Density Functional Theory Calculations for the ThMA, ThFA, and pFBA $CsPbI_3$ 2DRP Analogues

	C^{2D}_x [a]	C^{2D}_y [a]	E_{xVBM} [b]	E_{yVBM} [b]	E_{xCBM} [b]	E_{yCBM} [b]	μ_{ex} [c]	μ_{ey} [c]	μ_{hx} [c]	μ_{hy} [c]	τ_{ex} [d]	τ_{ey} [d]	τ_{hx} [d]	τ_{hy} [d]
ThMA	89.2	75.4	7.62	9.05	7.77	9.3	711.6	324.9	143.8	220.6	69.5	36.1	31.8	30.5
pFBA	73.2	81.7	8.65	9.07	8.52	9.04	104.9	196.2	172.2	199.0	22.0	30.0	27.8	30.1
ThFA	97.4	65.4	8.4	8.27	6.87	8.18	1629.4	351.5	459.2	269.1	124.2	39.7	53.9	34.4

[a]In units of newtons per meter. [b]In units of electronvolts. [c]In units of square centimeters per volt per second. [d]In units of femtoseconds.

https://doi.org/10.1021/acs.jpclett.2c03463
J. Phys. Chem. Lett. 2022, 13, 12090−12098

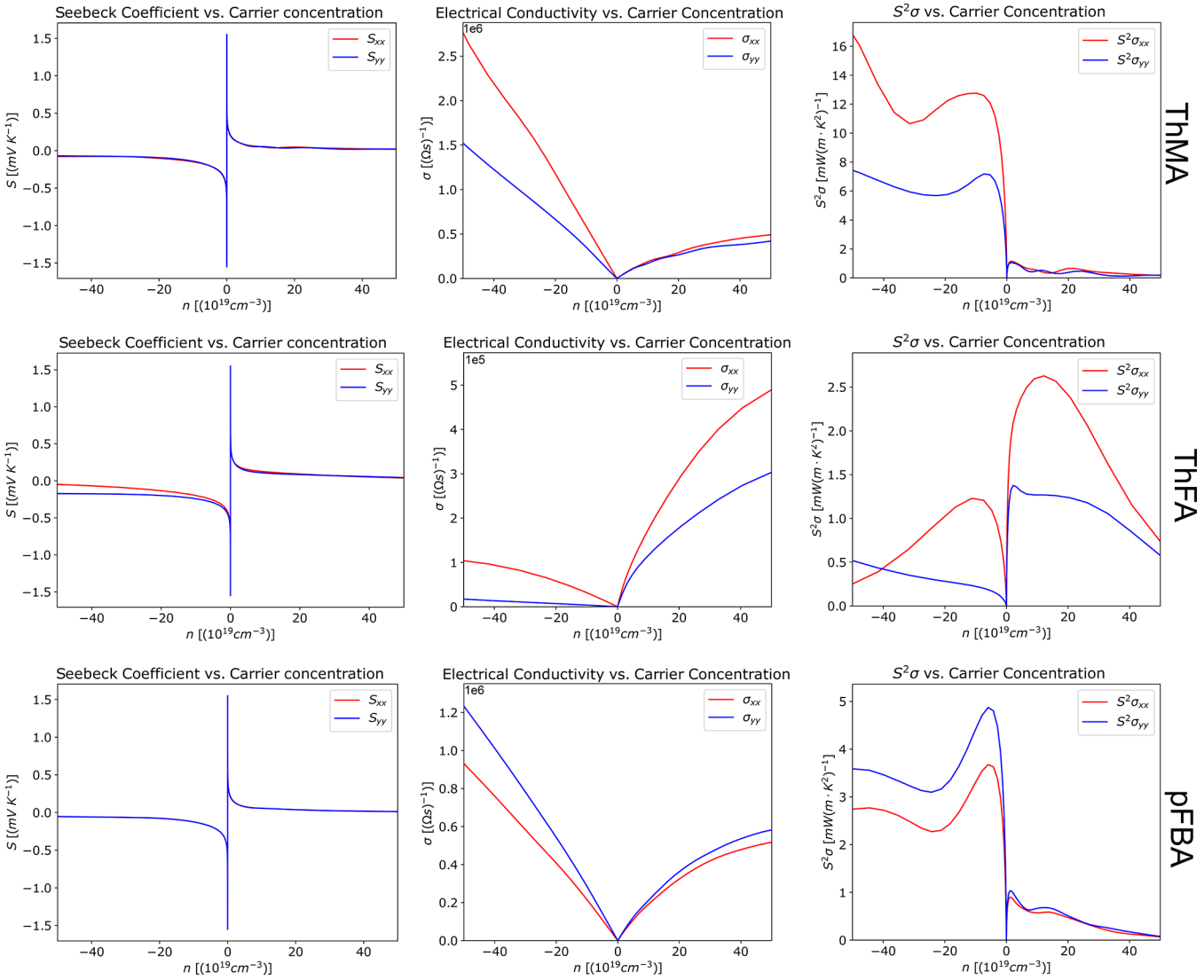

Figure 5. Seebeck coefficients, electrical conductivities, and TE power factors for the ThMA, ThFA, and pFBA CsPbI3 2DRP analogues.

In conclusion, we present a broad computational investigation of the differences in 2DRP $CsPbI_3$ analogues that can be attributed to the A′ spacer by considering ThMA, ThFA, and pFBA aromatic cations. We find that band alignment in the ThFA perovskite leads to a smaller band gap because of the strong localization of electronic states to the spacer at the conduction band edge. Additionally, investigating the potential of the three perovskites for TE applications revealed that the introduction of midgap states, such as those seen in the ThFA-containing perovskite, largely restrict effective TE transport properties if they come in the form of localized, nondispersive bands. Finally, we uncover the key geometric differences associated with both the organic−inorganic interactions, attributable largely to the differing NH−I interactions across the three spacers, and the organic−organic interactions associated with the aromatic rings far from the inorganic layers. These properties can be used to aid in the selection of organic spacers that generate robust and tunable 2DPKs for highly tailored applications.

METHODS

All density functional theory (DFT) calculations were computed using the GPAW package, employing PAW pseudopotentials for the description of core electrons, the PBE exchange-correlation functional, and a plane-wave basis with a kinetic energy cutoff of 600 eV for valence electrons.[58,59] Self-consistent field calculations were carried out to within 0.5 meV/valence electron and 10^{-4} e/valence electron for the energy and density, respectively. Geometry optimizations were carried out until the minimum force did not exceed 0.02 eV/Å, and all subsequent geometric analysis was done using the Atomic Simulation Environment.[60] Ground state properties were computed on a 6 × 6 × 1 k-point grid, and subsequent band structures were computed with 170 k-points along the high-symmetry path, with unoccupied eigenstates converged up to 2 eV above the CBM. BoltzTraP2 was used for interpolation of the band structure with an input 10 × 10 × 2 grid and was converged with respect to the DFT-computed band structure prior to computation of TE properties.[61] Effective masses were computed using the effmass code for the SOC and non-SOC band structures, where SOC is included with the method described by Olsen in the GPAW package.[62,63] In-plane stiffness constants and deformation potentials were computed using a relaxed ion approach in which uniaxial strain is applied, followed by a fixed cell geometry optimization.[64] Stiffness constants and deformation

https://doi.org/10.1021/acs.jpclett.2c03463
J. Phys. Chem. Lett. 2022, 13, 12090−12098

potentials were computed using a relaxed ion approach; fits of energy versus strain curves are available in the Supporting Information.

■ ASSOCIATED CONTENT

Supporting Information

The Supporting Information is available free of charge at https://pubs.acs.org/doi/10.1021/acs.jpclett.2c03463.

Fractional coordinates and cell parameters for the ThMA-, ThFA-, and pFBA-containing perovskites, geometric information regarding the relevant bond angles and bond distances, plots of the density of states, dense SOC band structure along the Γ−X−Y path, and the data used to fit quantities obtained with the deformation potential theory (PDF)

■ AUTHOR INFORMATION

Corresponding Author

Dhara J. Trivedi − *Department of Physics, Clarkson University, Potsdam, New York 13699, United States;* orcid.org/0000-0002-8151-3929; Email: dtrivedi@clarkson.edu

Author

Robert Stanton − *Department of Physics, Clarkson University, Potsdam, New York 13699, United States;* orcid.org/0000-0002-4989-6958

Complete contact information is available at: https://pubs.acs.org/10.1021/acs.jpclett.2c03463

Notes

The authors declare no competing financial interest.

■ ACKNOWLEDGMENTS

The authors gratefully acknowledge support from the U.S. National Science Foundation (ECCS-2138728).

■ ABBREVIATIONS

PV, photovoltaic; TE, thermoelectric; RP, Ruddlesden−Popper; ThMA, 2-thiophenemethylamine; ThFA, 2-thiopheneformamidine; pFBA, *p*-benzylammonium; PCE, power conversion efficiency; 2DPK, two-dimensional perovskite; 2DRP, 2D Ruddlesden−Popper; VBM, valence band maximum; CBM, conduction band minimum; PDOS, projected density of states; SOC, spin−orbit coupling.

■ REFERENCES

(1) Zhang, G.; Liu, G.; Wang, L.; Irvine, J. T. S. Inorganic Perovskite Photocatalysts for Solar Energy Utilization. *Chem. Soc. Rev.* **2016**, *45* (21), 5951−5984.

(2) Park, N. G. Research Direction toward Scalable, Stable, and High Efficiency Perovskite Solar Cells. *Adv. Energy Mater.* **2020**, *10* (13), 1903106.

(3) Yin, W. J.; Shi, T.; Yan, Y. Unique Properties of Halide Perovskites as Possible Origins of the Superior Solar Cell Performance. *Adv. Mater.* **2014**, *26* (27), 4653−4658.

(4) Zhang, L.; Liang, W. How the Structures and Properties of Two-Dimensional Layered Perovskites MAPbI3 and CsPbI3 Vary with the Number of Layers. *J. Phys. Chem. Lett.* **2017**, *8* (7), 1517−1523.

(5) Roy, P.; Kumar Sinha, N.; Tiwari, S.; Khare, A. A Review on Perovskite Solar Cells: Evolution of Architecture, Fabrication Techniques, Commercialization Issues and Status. *Sol. Energy* **2020**, *198*, 665−688.

(6) Gharibzadeh, S.; Hossain, I. M.; Fassl, P.; Nejand, B. A.; Abzieher, T.; Schultes, M.; Ahlswede, E.; Jackson, P.; Powalla, M.; Schäfer, S.; Rienäcker, M.; Wietler, T.; Peibst, R.; Lemmer, U.; Richards, B. S.; Paetzold, U. W. 2D/3D Heterostructure for Semitransparent Perovskite Solar Cells with Engineered Bandgap Enables Efficiencies Exceeding 25% in Four-Terminal Tandems with Silicon and CIGS. *Adv. Funct. Mater.* **2020**, *30* (19), 1909919.

(7) Wang, R.; Mujahid, M.; Duan, Y.; Wang, Z. K.; Xue, J.; Yang, Y. A Review of Perovskites Solar Cell Stability. *Adv. Funct. Mater.* **2019**, *29* (47), 1808843.

(8) Krishnan, U. Factors Affecting the Stability of Perovskite Solar Cells: A Comprehensive Review. *J. Photonics Energy* **2019**, *9* (02), 1.

(9) Urbina, A. The Balance between Efficiency, Stability and Environmental Impacts in Perovskite Solar Cells: A Review. *JPhys Energy* **2020**, *2* (2), 022001.

(10) Dou, J.; Bai, Y.; Chen, Q. Challenges of Lead Leakage in Perovskite Solar Cells. *Mater. Chem. Front.* **2022**, *6* (19), 2779−2789.

(11) Li, X.; Zhang, F.; He, H.; Berry, J. J.; Zhu, K.; Xu, T. On-Device Lead Sequestration for Perovskite Solar Cells. *Nature* **2020**, *578* (7796), 555−558.

(12) Chen, S.; Deng, Y.; Xiao, X.; Xu, S.; Rudd, P. N.; Huang, J. Preventing Lead Leakage with Built-in Resin Layers for Sustainable Perovskite Solar Cells. *Nat. Sustain.* **2021**, *4* (7), 636−643.

(13) Niu, B.; Wu, H.; Yin, J.; Wang, B.; Wu, G.; Kong, X.; Yan, B.; Yao, J.; Li, C. Z.; Chen, H. Mitigating the Lead Leakage of High-Performance Perovskite Solar Cells via in Situ Polymerized Networks. *ACS Energy Lett.* **2021**, *6* (10), 3443−3449.

(14) Wu, S.; Li, Z.; Li, M. Q.; Diao, Y.; Lin, F.; Liu, T.; Zhang, J.; Tieu, P.; Gao, W.; Qi, F.; Pan, X.; Xu, Z.; Zhu, Z.; Jen, A. K. Y. 2D Metal−Organic Framework for Stable Perovskite Solar Cells with Minimized Lead Leakage. *Nat. Nanotechnol.* **2020**, *15* (11), 934−940.

(15) Blancon, J. C.; Even, J.; Stoumpos, C. C.; Kanatzidis, M. G.; Mohite, A. D. Semiconductor Physics of Organic−Inorganic 2D Halide Perovskites. *Nat. Nanotechnol.* **2020**, *15* (12), 969−985.

(16) Liu, Z.; Yang, H.; Wang, J.; Yuan, Y.; Hills-Kimball, K.; Cai, T.; Wang, P.; Tang, A.; Chen, O. Synthesis of Lead-Free Cs2AgBix6 (X = Cl, Br, I) Double Perovskite Nanoplatelets and Their Application in CO2 Photocatalytic Reduction. *Nano Lett.* **2021**, *21* (4), 1620−1627.

(17) Cong, M.; Zhang, Q.; Yang, B.; Chen, J.; Xiao, J.; Zheng, D.; Zheng, T.; Zhang, R.; Qing, G.; Zhang, C.; Han, K. L. Bright Triplet Self-Trapped Excitons to Dopant Energy Transfer in Halide Double-Perovskite Nanocrystals. *Nano Lett.* **2021**, *21* (20), 8671−8678.

(18) Zhao, X.; Liu, T.; Kaplan, A. B.; Yao, C.; Loo, Y. L. Accessing Highly Oriented Two-Dimensional Perovskite Films via Solvent-Vapor Annealing for Efficient and Stable Solar Cells. *Nano Lett.* **2020**, *20* (12), 8880−8889.

(19) Chen, P.; Bai, Y.; Wang, S.; Lyu, M.; Yun, J. H.; Wang, L. In Situ Growth of 2D Perovskite Capping Layer for Stable and Efficient Perovskite Solar Cells. *Adv. Funct. Mater.* **2018**, *28* (17), 1706923.

(20) Zhou, X.; Jankowska, J.; Dong, H.; Prezhdo, O. V. Recent Theoretical Progress in the Development of Perovskite Photovoltaic Materials. *J. Energy Chem.* **2018**, *27* (3), 637−649.

(21) Dyksik, M.; Duim, H.; Zhu, X.; Yang, Z.; Gen, M.; Kohama, Y.; Adjokatse, S.; Maude, D. K.; Loi, M. A.; Egger, D. A.; Baranowski, M.; Plochocka, P. Broad Tunability of Carrier Effective Masses in Two-Dimensional Halide Perovskites. *ACS Energy Lett.* **2020**, *5* (11), 3609−3616.

(22) Li, Y.; Milić, J. V.; Ummadisingu, A.; Seo, J. Y.; Im, J. H.; Kim, H. S.; Liu, Y.; Dar, M. I.; Zakeeruddin, S. M.; Wang, P.; Hagfeldt, A.; Grätzel, M. Bifunctional Organic Spacers for Formamidinium-Based Hybrid Dion-Jacobson Two-Dimensional Perovskite Solar Cells. *Nano Lett.* **2019**, *19* (1), 150−157.

(23) Tang, G.; Wang, V.; Zhang, Y.; Ghosez, P.; Hong, J. Orbital−energy Splitting in Ruddlesden−Popper Layered Halide Perovskites for Tunable Optoelectronic Properties. *J. Power Sources* **2021**, *514*, 230546.

(24) Wu, K.; Chen, J.; Ma, H.; Wan, L.; Hu, W.; Yang, J. Two-Dimensional Giant Tunable Rashba Semiconductors with Two-Atom-

Thick Buckled Honeycomb Structure. *Nano Lett.* **2021**, *21* (1), 740−746.
(25) Kang, S.; Lee, D.; Kim, J.; Capasso, A.; Kang, H. S.; Park, J. W.; Lee, C. H.; Lee, G. H. 2D Semiconducting Materials for Electronic and Optoelectronic Applications: Potential and Challenge. *2D Mater.* **2020**, *7* (2), 022003.
(26) Fang, C.; Wang, H.; Li, D. Recent Progress in Two-Dimensional Ruddlesden−Popper Perovskite Based Heterostructures. *2D Mater.* **2021**, *8* (2), 022006.
(27) Xia, C. X.; Du, J.; Huang, X. W.; Xiao, W. B.; Xiong, W. Q.; Wang, T. X.; Wei, Z. M.; Jia, Y.; Shi, J. J.; Li, J. B. Two-Dimensional n-InSe/ p-GeSe(SnS) van Der Waals Heterojunctions: High Carrier Mobility and Broadband Performance. *Phys. Rev. B* **2018**, *97* (11), 1−9.
(28) Perez, C. M.; Ghosh, D.; Prezhdo, O.; Nie, W.; Tretiak, S.; Neukirch, A. Point Defects in Two-Dimensional Ruddlesden−Popper Perovskites Explored with Ab Initio Calculations. *J. Phys. Chem. Lett.* **2022**, 5213−5219.
(29) Baranowski, M.; Surrente, A.; Plochocka, P. Two Dimensional Perovskites/Transition Metal Dichalcogenides Heterostructures: Puzzles and Challenges. *Isr. J. Chem.* **2022**, *62* (3−4), 1−14.
(30) Lee, J.; Lee, W.; Kang, K.; Lee, T.; Lee, S. K. Layer-by-Layer Structural Identification of 2D Ruddlesden-Popper Hybrid Lead Iodide Perovskites by Solid-State NMR Spectroscopy. *Chem. Mater.* **2021**, *33* (1), 370−377.
(31) Luo, T.; Zhang, Y.; Xu, Z.; Niu, T.; Wen, J.; Lu, J.; Jin, S.; Liu, S.; Zhao, K. Compositional Control in 2D Perovskites with Alternating Cations in the Interlayer Space for Photovoltaics with Efficiency over 18%. *Adv. Mater.* **2019**, *31* (44), 1903848.
(32) Zhou, N.; Huang, B.; Sun, M.; Zhang, Y.; Li, L.; Lun, Y.; Wang, X.; Hong, J.; Chen, Q.; Zhou, H. The Spacer Cations Interplay for Efficient and Stable Layered 2D Perovskite Solar Cells. *Adv. Energy Mater.* **2020**, *10* (1), 1901566.
(33) Zhao, X.; Liu, T.; Loo, Y. L. Advancing 2D Perovskites for Efficient and Stable Solar Cells: Challenges and Opportunities. *Adv. Mater.* **2022**, *34* (3), 2105849.
(34) Zhang, F.; Kim, D. H.; Zhu, K. 3D/2D Multidimensional Perovskites: Balance of High Performance and Stability for Perovskite Solar Cells. *Curr. Opin. Electrochem.* **2018**, *11*, 105−113.
(35) Stanton, R.; Gupta, S. K.; Trivedi, D. J. Probing Strain-Induced Effects on Performance of Low-Dimensional Hybrid Perovskites for Solar Energy Harvesting. *ACS Appl. Mater. Interfaces* **2022**, *14* (30), 34603−34611.
(36) Etienne, T.; Mosconi, E.; De Angelis, F. Dynamical Origin of the Rashba Effect in Organohalide Lead Perovskites: A Key to Suppressed Carrier Recombination in Perovskite Solar Cells? *J. Phys. Chem. Lett.* **2016**, *7* (9), 1638−1645.
(37) Huang, G.; Rassel, S.; Qu, J.; Xu, S.; Wang, C.; Ban, D. Manipulation of Spin Splitting in Two-Dimensional Lead Bromide Perovskite Rashba Piezoelectrics. *ACS Appl. Electron. Mater.* **2021**, *3* (1), 285−291.
(38) Li, X.; Hoffman, J. M.; Kanatzidis, M. G. The 2D Halide Perovskite Rulebook: How the Spacer Influences Everything from the Structure to Optoelectronic Device Efficiency. *Chem. Rev.* **2021**, *121* (4), 2230−2291.
(39) Zhao, R.; Sabatini, R. P.; Zhu, T.; Wang, S.; Morteza Najjarian, A.; Johnston, A.; Lough, A. J.; Hoogland, S.; Sargent, E. H.; Seferos, D. S. Rigid Conjugated Diamine Templates for Stable Dion-Jacobson-Type Two-Dimensional Perovskites. *J. Am. Chem. Soc.* **2021**, *143* (47), 19901−19908.
(40) Gao, Y.; Sachinthani, K. A. N.; Zheng, C.; Jarrett-Wilkins, C.; Johnston, A.; Sun, M. J.; Najarian, A. M.; Wang, Y. K.; Saidaminov, M. I.; de Arquer, F. P. G.; Seferos, D. S.; Hoogland, S.; Sargent, E. H. Self-Aligned Non-Centrosymmetric Conjugated Molecules Enable Electro-Optic Perovskites. *Adv. Opt. Mater.* **2021**, *9* (20), 2100730.
(41) Guo, Y.; Yaffe, O.; Paley, D. W.; Beecher, A. N.; Hull, T. D.; Szpak, G.; Owen, J. S.; Brus, L. E.; Pimenta, M. A. Interplay between Organic Cations and Inorganic Framework and Incommensurability in Hybrid Lead-Halide Perovskite CH3NH3PbBr3. *Phys. Rev. Mater.* **2017**, *1* (4), 1−6.
(42) Xu, Z.; Li, L.; Dong, X.; Lu, D.; Wang, R.; Yin, W.-J.; Liu, Y. CsPbI3-Based Phase-Stable 2D Ruddlesden−Popper Perovskites for Efficient Solar Cells. *Nano Lett.* **2022**, *22* (7), 2874−2880.
(43) Yan, G.; Sui, G.; Chen, W.; Su, K.; Feng, Y.; Zhang, B. Selectively Fluorinated Benzylammonium-Based Spacer Cation Enables Graded Quasi-2D Perovskites for Efficient and Stable Solar Cells. *Chem. Mater.* **2022**, *34* (7), 3346−3356.
(44) Zibouche, N.; Islam, M. S. Structure-Electronic Property Relationships of 2D Ruddlesden-Popper Tin- And Lead-Based Iodide Perovskites. *ACS Appl. Mater. Interfaces* **2020**, *12* (13), 15328−15337.
(45) Leveillee, J.; Katan, C.; Even, J.; Ghosh, D.; Nie, W.; Mohite, A. D.; Tretiak, S.; Schleife, A.; Neukirch, A. J. Tuning Electronic Structure in Layered Hybrid Perovskites with Organic Spacer Substitution. *Nano Lett.* **2019**, *19* (12), 8732−8740.
(46) Tofanello, A.; Freitas, A. L. M.; de Queiroz, T. B.; Bonadio, A.; Martinho, H.; Souza, J. A. Magnetism in a 2D Hybrid Ruddlesden-Popper Perovskite through Charge Redistribution Driven by an Organic Functional Spacer. *J. Phys. Chem. Lett.* **2022**, *13* (6), 1406−1415.
(47) Long, M.; Zhang, T.; Chen, D.; Qin, M.; Chen, Z.; Gong, L.; Lu, X.; Xie, F.; Xie, W.; Chen, J.; Xu, J. Interlayer Interaction Enhancement in Ruddlesden-Popper Perovskite Solar Cells toward High Efficiency and Phase Stability. *ACS Energy Lett.* **2019**, *4* (5), 1025−1033.
(48) Prasanna, R.; Gold-Parker, A.; Leijtens, T.; Conings, B.; Babayigit, A.; Boyen, H. G.; Toney, M. F.; McGehee, M. D. Band Gap Tuning via Lattice Contraction and Octahedral Tilting in Perovskite Materials for Photovoltaics. *J. Am. Chem. Soc.* **2017**, *139* (32), 11117−11124.
(49) Pious, J. K.; Muthu, C.; Vijayakumar, C. Organic Spacer Cation Assisted Modulation of the Structure and Properties of Bismuth Halide Perovskites. *Acc. Chem. Res.* **2022**, *55* (3), 275−285.
(50) Kim, Y. S.; Ri, C. H.; Kye, Y. H.; Jong, U. G.; Yu, C. J. Improving the Stability of Hybrid Perovskite FAPbI3 by Forming 3D/2D Interfaces with Organic Spacers. *ChemComm* **2022**, *58* (60), 8440−8443.
(51) Yin, W. J.; Shi, T.; Yan, Y. Superior Photovoltaic Properties of Lead Halide Perovskites: Insights from First-Principles Theory. *J. Phys. Chem. C* **2015**, *119* (10), 5253−5264.
(52) Wang, T.; Daiber, B.; Frost, J. M.; Mann, S. A.; Garnett, E. C.; Walsh, A.; Ehrler, B. Indirect to Direct Bandgap Transition in Methylammonium Lead Halide Perovskite. *Energy Environ. Sci.* **2017**, *10* (2), 509−515.
(53) Yan, J.; Mortensen, J. J.; Jacobsen, K. W.; Thygesen, K. S. Linear Density Response Function in the Projector Augmented Wave Method: Applications to Solids, Surfaces, and Interfaces. *Phys. Rev. B - Condens. Matter Mater. Phys.* **2011**, *83* (24), 1−10.
(54) Abdallah, I. O.; Joubert, D. P.; Suleiman, M. S. H. Investigation of Thermoelectric Properties of CH3NH3PbI3: Density Functional Theory and Boltzmann Transport Calculations. *SA Inst. Phys.* **2018**, 2−7.
(55) Glavin, N. R.; Rao, R.; Varshney, V.; Bianco, E.; Apte, A.; Roy, A.; Ringe, E.; Ajayan, P. M. Emerging Applications of Elemental 2D Materials. *Adv. Mater.* **2020**, *32* (7), 1904302.
(56) Haque, M. A.; Kee, S.; Villalva, D. R.; Ong, W. L.; Baran, D. Halide Perovskites: Thermal Transport and Prospects for Thermoelectricity. *Adv. Sci.* **2020**, *7* (10), 1903389.
(57) Hsu, S. N.; Zhao, W.; Gao, Y.; Akriti; Segovia, M.; Xu, X.; Boudouris, B. W.; Dou, L. Thermoelectric Performance of Lead-Free Two-Dimensional Halide Perovskites Featuring Conjugated Ligands. *Nano Lett.* **2021**, *21*, 7839.
(58) Enkovaara, J.; Rostgaard, C.; Mortensen, J. J.; Chen, J.; Dułak, M.; Ferrighi, L.; Gavnholt, J.; Glinsvad, C.; Haikola, V.; Hansen, H. A.; Kristoffersen, H. H.; Kuisma, M.; Larsen, A. H.; Lehtovaara, L.; Ljungberg, M.; Lopez-Acevedo, O.; Moses, P. G.; Ojanen, J.; Olsen, T.; Petzold, V.; Romero, N. A.; Stausholm-Møller, J.; Strange, M.; Tritsaris, G. A.; Vanin, M.; Walter, M.; Hammer, B.; Häkkinen, H.;

https://doi.org/10.1021/acs.jpclett.2c03463
J. Phys. Chem. Lett. 2022, 13, 12090−12098

Madsen, G. K. H.; Nieminen, R. M.; Nørskov, J. K.; Puska, M.; Rantala, T. T.; Schiøtz, J.; Thygesen, K. S.; Jacobsen, K. W. Electronic Structure Calculations with GPAW: A Real-Space Implementation of the Projector Augmented-Wave Method. *J. Phys.: Condens. Matter* **2010**, *22* (25), 253202.
(59) Mortensen, J. J.; Hansen, L. B.; Jacobsen, K. W. Real-Space Grid Implementation of the Projector Augmented Wave Method. *Phys. Rev. B - Condens. Matter Mater. Phys.* **2005**, *71* (3), 1−11.
(60) Hjorth Larsen, A.; Jørgen Mortensen, J.; Blomqvist, J.; Castelli, I. E.; Christensen, R.; Dułak, M.; Friis, J.; Groves, M. N.; Hammer, B.; Hargus, C.; Hermes, E. D.; Jennings, P. C.; Bjerre Jensen, P.; Kermode, J.; Kitchin, J. R.; Leonhard Kolsbjerg, E.; Kubal, J.; Kaasbjerg, K.; Lysgaard, S.; Bergmann Maronsson, J.; Maxson, T.; Olsen, T.; Pastewka, L.; Peterson, A.; Rostgaard, C.; Schiøtz, J.; Schütt, O.; Strange, M.; Thygesen, K. S.; Vegge, T.; Vilhelmsen, L.; Walter, M.; Zeng, Z.; Jacobsen, K. W. The Atomic Simulation Environment—a Python Library for Working with Atoms. *J. Phys.: Condens. Matter* **2017**, *29* (27), 273002.
(61) Madsen, G. K. H.; Carrete, J.; Verstraete, M. J. BoltzTraP2, a Program for Interpolating Band Structures and Calculating Semi-Classical Transport Coefficients. *Comput. Phys. Commun.* **2018**, *231*, 140−145.
(62) Whalley, L. D. wffmass: An Effective Mass Package. *Journal of Open Source Software* **2018**, *3* (28), 797.
(63) Olsen, T. Designing In-Plane Heterostructures of Quantum Spin Hall Insulators from First Principles: 1 T′-MoS2 with Adsorbates. *Phys. Rev. B* **2016**, *94*, 235106.
(64) Kumavat, S. R.; Sonvane, Y.; Singh, D.; Gupta, S. K. Two-Dimensional CH3NH3PbI3 with High Efficiency and Superior Carrier Mobility: A Theoretical Study. *J. Phys. Chem. C* **2019**, *123* (9), 5231−5239.

https://doi.org/10.1021/acs.jpclett.2c03463
J. Phys. Chem. Lett. 2022, 13, 12090−12098